International Forum on Aeroelasticity and Structural Dynamics
IFASD 2022
13-17 June 2022, Madrid, Spain

MODEL SELECTION FOR A MULTIPLE-MODEL ADAPTIVE GUST LOAD ALLEVIATION CONTROLLER

Matthias Wüstenhagen[1]

[1]Institute of System Dynamics and Control, German Aerospace Center (DLR)
Münchener Straße 20, 82234 Weßling, Germany
matthias.wuestenhagen@dlr.de

Keywords: Flexible aircraft, multiple-model adaptive control, gust load alleviation, aeroelasticity

Abstract: Today's advanced aircraft designs with respect to new materials and high aspect ratio wings demand for improved control algorithms solving specific issues arising from the new technologies. In this paper, a multiple-model adaptive gust load alleviation control system for a two-degree-of-freedom aerofoil model and a flexible demonstrator aircraft is discussed to augment aircraft of increased vulnerability to gust encounter. Multiple-model adaptive control provides the possibility to improve the performance when a crucial change in system parameters is expected. For the two example cases sets of discrete mass conditions are defined representing various fuel levels. Gust load alleviation controllers are synthesised for each mass case and compared to a reference controller robustly synthesised over the entire range of mass properties. Subsequently, a minimum amount of controllers necessary to achieve the performance benefit of multiple-model adaptive control is selected.

1 INTRODUCTION

The fuel costs account for the greatest portion of the operating costs of today's aircraft. That is why fuel efficiency is one of the most relevant aspects of new aircraft designs [1]. Lightweight wing structures and higher aspect ratios hold a crucial potential to enhance the fuel efficiency and make flying more economic. However, the wings tend to be more flexible which makes unstable phenomena like flutter more likely to occur and increases the demand for active flutter suppression (AFS) [2]. Furthermore, these aircraft are more vulnerable to loads caused by manoeuvres and gusts [3, 4]. Active manoeuvre load alleviation (MLA), like demonstrated in Refs. [5, 6], decreases the wing loads during manoeuvres. In constrast, with active gust load alleviation (GLA) the loads due to gust encounter can be reduced [7–10]. The synthesis of MLA or GLA controllers, however, is demanding as structurally more efficient aircraft lack a clear separation of rigid body and flexible modes [4].
Within the Horizon 2020 project *Flight Phase Adaptive Aero-Servo-Elastic aircraft Design methods* (FliPASED) secondary control systems for flexible aircraft, e.g. active GLA, are synthesised and tested on the demonstrator aircraft depicted in Figure 1 [11]. Further details on the modelling, primary and secondary flight control synthesis and flight testing of the demonstrator aircraft can be found in Refs. [13–17]. For the synthesis of a GLA controller aeroelastic models are generated. Often these are linearised state-space systems defined at specific operating points within the flight envelope [7, 9, 10, 18]. However, significant changes in system parameters may not be adequately covered by a linearised model and therefore the controller might not be robust [19]. Adaptive control techniques offer the possibility to adapt the controller to the

Figure 1: FliPASED demonstrator aircraft [12].

prevailing flight conditions during the aircraft's operation and ensure optimal performance over a large range of operational conditions [19]. The simplest form of an adaptive control technique is gain-scheduling where a change in parameters, e.g. airspeed, is measured and used to adapt the controller by means of interpolation within a grid of controllers [19]. There exists quite a rich literature on gain-scheduling techniques applied to flight control problems [20–22]. It is necessary for gain-scheduling that the scheduling parameter is directly measurable. However, the system dynamics might also change due to parameters which cannot be easily measured. In this paper, the deviation in mass distribution, which depends on the fuel level, is followed. Especially when tanks are located in the wings, a variation of the flexible mode shapes is the consequence [23]. Besides, deviations could also be provoked by uncertainties due to unmodelled dynamics or non-linearities in aerodynamic parameters, mass, damping and stiffness matrices and many more. In any of the mentioned cases the system behaviour needs to be somehow estimated. Indirect adaptive control allows to estimate the current plant parameters with respect to the onboard measurements. The identified parameters then lead to the controller gains. For the estimation of the plant parameters, however, the excitation of the system needs to be rich enough in its spectrum to guarantee convergence of the parameters [19]. Direct model reference adaptive control (MRAC) requires a reference model providing the desired system output. The difference between the real system measurements and the reference model outputs yields a residual used for control gain update [19]. A major limitation of direct MRAC is its sensitivity to process and sensor noise in the presence of unmodelled dynamics [24]. For multiple-model adaptive control (MMAC), illustrated in Figure 2, the deviation in the system $p(t)$ is covered by N discrete intermediate models. By means of estimators the model that represents the plant behaviour best is then identified. Subsequently, MMAC switches to the corresponding controller. Generally, there exist several scientific studies on MMAC [19, 23, 25–27].

As the mass distribution cannot be directly measured, but its deviation over time is approximately known, in this paper, the focus is on MMAC. The main question addressed is "How to select the discrete mass models?". The model estimation and switching of controllers will be part of further research. To answer the question on model selection the gust loads of an aerofoil model and of the FliPASED demonstrator aircraft are examined with respect to a changing mass distribution caused by fuel consumption. For the selection of suitable models Refs. [28,29] propose to look at the steady state outputs of the system over the regarded range of parameter changes. Thus, a set of linear models following a piecewise linear trend in the output variables can be identified. In Ref. [30] the answer is linked to the control synthesis itself as the ν-gap metric of closed-loop systems with respect to different mass cases is analysed. Ref. [27] follows an even more pragmatic approach. Finely gridding the range of parameters and synthesising a controller for each parameter value a maximum achievable performance with MMAC is provided. Subsequently, it is decided on how the number of models and corresponding controllers can be reduced without dropping below a performance bound. In this paper, the approach from Ref. [27] is slightly adapted for the selection of the mass cases for GLA control. The GLA control synthesis is defined as an optimisation problem over a family of gust encounters, like in

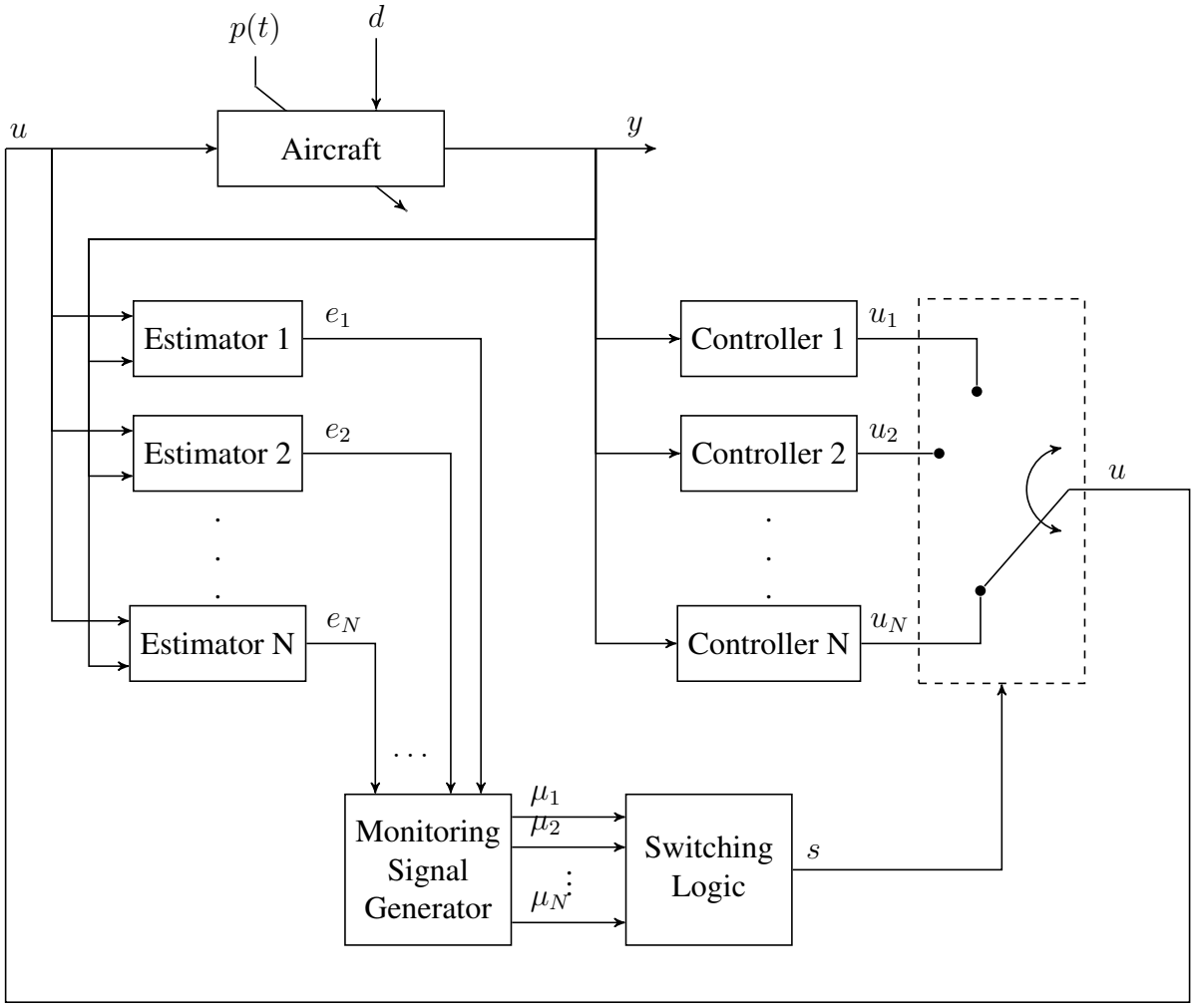

Figure 2: MMAC architecture.

Ref. [31].
Firstly, the aeroelastic modelling process is described in section 2. The GLA control synthesis is depicted in section 3. Finally, section 4 summarises the results of the GLA controller synthesis and controller selection.

2 MODELLING

Two different models are examined in detail with respect to gust encounter. Firstly, a very fundamental aerofoil section model is set up, as it allows fast adaption and exhibits a short simulation and control synthesis time. Secondly, a study on the FliPASED demonstrator aircraft model is undertaken. For both varying mass properties p_m are considered. They are limited to the compact set

$$\Omega_{p_m} = \{p_m : p_{m,\text{low}} \leq p_m \leq p_{m,\text{high}}\} \tag{1}$$

with the lowest and highest mass properties $p_{m,\text{low}}$ and $p_{m,\text{high}}$ [27]. However, for the subsequent examinations it is more convenient to use a discrete set

$$\tilde{\Omega}_{p_m} = \{p_{m,i} : p_{m,\text{low}} \leq p_{m,i} \leq p_{m,\text{high}},\ \forall i = 1, ..., n_m\},\ \tilde{\Omega}_{p_m} \subseteq \Omega_{p_m}, \tag{2}$$

where $p_{m,i}$ indicates the i^{th} of n_m discrete, intermediate mass cases. These mass cases can then be combined as a sequence of linear time-invariant (LTI) models by

$$\begin{aligned} \dot{x} &= A(p_{m,i})x + B(p_{m,i})u \\ y &= C(p_{m,i})x + D(p_{m,i})u. \end{aligned} \tag{3}$$

In Equation (3), $A(p_{m,i})$, $B(p_{m,i})$, $C(p_{m,i})$ and $D(p_{m,i})$ are the mass property dependent state-space matrices relating the inputs u, states x and outputs y with each other [32].

2.1 Aerofoil Model

The aerofoil model is a two-degree-of-freedom (DOF) model as it allows one translational and one angular motion, namely heave and pitch [33, 34]. Unsteady aerodynamics are neglected leading to a steady aerodynamic model. A detailed representation of the aerofoil is illustrated in Figure 3. The dynamics of the aerofoil describe an equilibrium of forces and moments at the

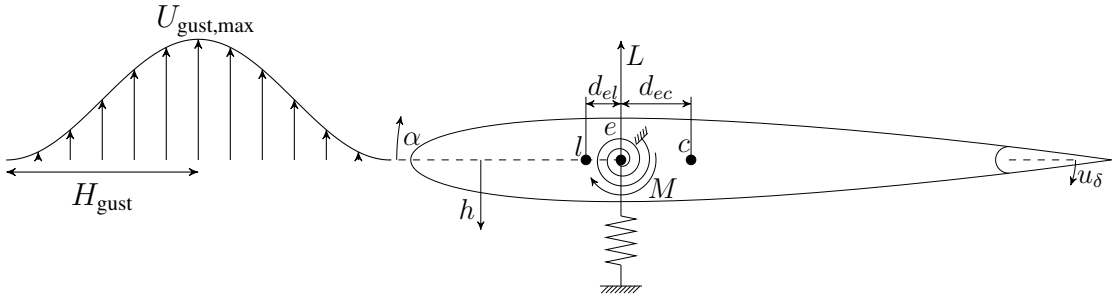

Figure 3: Aerofoil model [33, 34].

elastic axi es. The governing equations are

$$\underbrace{\begin{bmatrix} m & md_{ec} \\ md_{ec} & J_\alpha \end{bmatrix}}_{M_{af}} \begin{bmatrix} \ddot{h} \\ \ddot{\alpha} \end{bmatrix} + \underbrace{\begin{bmatrix} b_h & 0 \\ 0 & b_\alpha \end{bmatrix}}_{B_{af}} \begin{bmatrix} \dot{h} \\ \dot{\alpha} \end{bmatrix} + \underbrace{\begin{bmatrix} k_h & 0 \\ 0 & k_\alpha \end{bmatrix}}_{K_{af}} \begin{bmatrix} h \\ \alpha \end{bmatrix} = \begin{bmatrix} -L \\ M \end{bmatrix}. \tag{4}$$

As only two DOFs are considered the model is restricted to contributions from the lift force L and pitching moment M. Due to the applied sign convention upwards acting lift forces are considered negative. The inertial forces and moments are depicted by the first term on the left side of Equation (4). They depend on the heaving and pitching accelerations $\ddot{h}$ and $\ddot{\alpha}$, as well as on the aerofoil mass matrix M_{af} with mass m, mass moment of inertia I_α and the offset d_{ec} between the centre of gravity and the elastic axis. Multiplying the heaving and pitching velocity $\dot{h}$ and $\dot{\alpha}$ with the matrix B_{af}, which contains the translational and angular damping values b_h and b_α, yields the damping force and moment. The last term on the left side of the equation represents the force and moment caused by the elasticity of the structure. The translational and torsional spring stiffness k_h and k_α, combined in matrix K_{af}, linearly map the heaving position h and the angle of attack α with L and M. The lift and pitching moment are given by

$$\begin{aligned} L &= \rho U_\infty^2 (c_r/2) c_{l\alpha} \left(\alpha + \dot{h}/U_\infty - d_{el} \frac{\dot{\alpha}}{U_\infty} \right) + \rho U_\infty^2 (c_r/2) c_{l\delta} u_\delta + \rho U_\infty (c_r/2) c_{l\alpha} u_g \\ M &= \rho U_\infty^2 (c_r/2)^2 c_{m\alpha} \left(\alpha + \dot{h}/U_\infty - d_{el} \frac{\dot{\alpha}}{U_\infty} \right) + \rho U_\infty^2 (c_r/2)^2 c_{m\delta} u_\delta + \rho U_\infty (c_r/2)^2 c_{m\alpha} u_g. \end{aligned} \tag{5}$$

featuring three different contributions. These comprise aerodynamic effects due to a change in the states α, $\dot{h}$ and $\dot{\alpha}$, the deflection of the control surface u_δ and the gust velocity profile u_g. The air density and true airspeed are defined with ρ and U_∞. The aerofoil chord length is c_r, while the distance between the elastic axis e and the $1/4$-chord point l is d_{el}. The aerodynamic coefficients $c_{l\alpha}$ and $c_{m\alpha}$ relate the angle of attack α with the lift force L and the pitching moment M, while $c_{l\delta}$ and $c_{m\delta}$ comprise the lift and moment distributions due to the deflection of the control surface u_δ. The moment coefficient $c_{m\alpha}$ is correlated with the lift coefficient $c_{l\alpha}$ by

$$c_{m\alpha} = \frac{d_{el}}{c} c_{l\alpha}. \tag{6}$$

In terms of gust encounters the loads P_h and P_α acting on the aerofoil are crucial. These depend on the stiffness forces and moments and are assessed by

$$\begin{bmatrix} P_h \\ P_\alpha \end{bmatrix} = - \begin{bmatrix} k_h & 0 \\ 0 & k_\alpha \end{bmatrix} \begin{bmatrix} h \\ \alpha \end{bmatrix}. \tag{7}$$

It is referred to the fact that the heaving and pitching loads P_h and P_α are given in a different coordinate system than L and M. The aerofoil is considered to be a section of the left wing of an aircraft. Thus, loads acting upwards or anti-clockwise are positive.
Eventually, Equations 4, 5 and 7 can be expressed as an LTI state-space model like in Equation (3). The aerofoil model is then linearised for decreasing mass m and likewise mass moment of inertia J_α values representing the fuel loss of the wing tanks. In total 22 different mass cases are set up. The chosen parameters are displayed in Table 1. The heaving load P_h of the aerofoil

Table 1: Mass cases for the aerofoil model.

Mass Case	Mass [kg]	Mass Moment of Inertia [kgm^2]
1	12.39	0.065
2	12.09	0.063
3	11.79	0.062
4	11.49	0.060
5	11.19	0.059
6	10.89	0.057
7	10.59	0.056
8	10.29	0.054
9	9.99	0.052
10	9.69	0.051
11	9.39	0.049
12	9.09	0.048
13	8.79	0.046
14	8.49	0.045
15	8.19	0.043
16	7.89	0.041
17	7.59	0.040
18	7.29	0.038
19	6.99	0.037
20	6.69	0.035
21	6.39	0.034
22	6.09	0.032

would mainly contribute to the wing root bending moment (WRBM). Therefore, in this paper the GLA control synthesis for the aerofoil focuses on the reduction of P_h.

2.2 FliPASED Demonstrator Aircraft Model

An aeroservoelastic model of the FliPASED demonstrator aircraft is set up. The coupling of the aerodynamics and structural dynamics is its centrepiece. A finite element (FE) model shapes the structural model which is reduced with the Guyan reduction [35, 36]. The resulting structural grid is presented in Figure 4 as red points. Subsequently, the equations of motion (EOMs) based

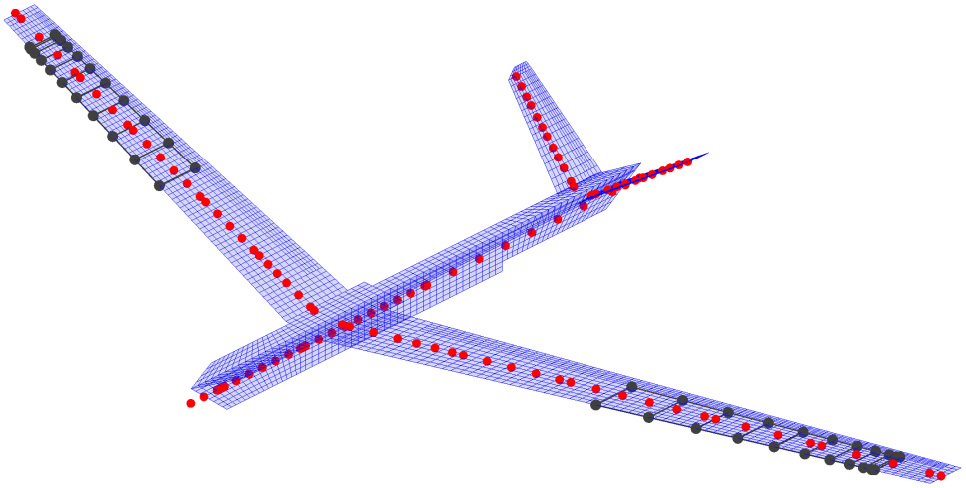

Figure 4: Structural grid and aerodynamic panels of the demonstrator aircraft [10].

on the assumptions listed in Ref. [10] are utilised. On the one hand, the non-linear Newton-Euler EOM

$$\begin{bmatrix} m_b(\dot{V}_b + \Omega_b \times V_b - T_{be} g_e) \\ J_b \dot{\Omega}_b + \Omega_b \times (J_b \Omega_b) \end{bmatrix} = \underbrace{\Phi_{gb}^T P_g^{\text{ext}}}_{P_b^{\text{ext}}} \tag{8}$$

represents the rigid body flight mechanics. The translational and angular velocities of the aircraft are given by V_b and Ω_b for the body frame of reference. The vector g_e is the gravitational acceleration transformed by T_{be} from the earth fixed to the body fixed frame of reference. The external loads P_g^{ext} acting on the structural grid points are multiplied with matrix Φ_{gb}^T transferring them to the rigid body frame of reference [36, 37]. On the other hand, the flexible motion relies on linear elastic theory with

$$M_{ff}\ddot{u}_f + B_{ff}\dot{u}_f + K_{ff}u_f = \underbrace{\Phi_{gf}^T P_g^{\text{ext}}(t)}_{P_f^{\text{ext}}(t)}, \tag{9}$$

where the generalised displacement u_f and its first and second derivatives $\dot{u}_f$ and $\ddot{u}_f$ are multiplied with the modal mass, damping or stiffness matrices M_{ff}, B_{ff} and K_{ff}. The modal matrix Φ_{gf} on the right-hand side contains the eigenvectors of the structural modes sorted according to their frequency [37]. Modal truncation is applied to reduce the DOFs for the most relevant eigenmodes [36].
The external loads P_g^{ext} combine the thrust and aerodynamic loads P_g^{eng} and P_g^{aero} yielding

$$P_g^{\text{ext}} = P_g^{\text{eng}} + P_g^{\text{aero}}. \tag{10}$$

The aerodynamic loads are determined with the doublet lattice method (DLM) combining steady and unsteady aerodynamic effects based on the panel model from Figure 4. As can

be seen, the lifting surfaces of the demonstrator aircraft are discretised by trapezoidal-shaped panels which contain doublets at the quarter-chord line. Subsequently, the pressure coefficient in the reduced frequency domain is determined at the $3/4$-chord line j by

$$\Delta c_{pj}(k) = Q_{jj}(k) w_j(k), \tag{11}$$

where $Q_{jj}(k)$ is the aerodynamic influence coefficient (AIC) matrix, $w_j(k)$ is the downwash and k is the reduced frequency

$$k = \omega \frac{c_r}{2U_\infty}. \tag{12}$$

In Equation (12) ω depicts the modal frequency, while c_r represents the reference chord length. When $k = 0$ the pressure coefficient $\Delta c_{pj}(k = 0)$ equals the quasi-steady aerodynamic solution [38].
The downwash w_j comprises various contributions yielding

$$w_j = w_{j,b_1} + w_{j,\mathrm{cs}_0} + w_{j,\mathrm{cs}_1} + w_{j,f_0} + w_{j,f_1} + w_{j,g_1}. \tag{13}$$

The term w_{j,b_1} depends on the velocity V_b and the angular velocity Ω_b and therefore results from the rigid body motion. The control surface deflections u_{cs} and deflection rates $\dot{u}_{\mathrm{cs}}$ result in w_{j,cs_0} and w_{j,cs_1}. The flexible motion defined by the modal deflection u_f and its derivative $\dot{u}_f$ lead to w_{j,f_0} and w_{j,f_1}. The contribution w_{j,g_1} is caused by gusts and atmospheric turbulence. Detailed information on how the contributions are determined is found in Refs. [37, 39].
In order to judge the performance of the demonstrator aircraft augmented by a GLA controller, the loads at the wing root are of special interest. However, unlike Equation (7) suggests it is not recommended to recover the loads the same way for the demonstrator aircraft. As modal truncation was applied earlier for the EOMs, determination of the WRBM P_{mx} via the stiffness matrix K_{ff} is inaccurate. Instead the force summation method (FSM) provides the wing root loads based on

$$P_{\mathrm{mx}} = T_{\mathrm{mx}g} \left(P_g^{\mathrm{ext}} - \underbrace{M_{gg} \begin{bmatrix} \Phi_{gb} & \Phi_{gf} \end{bmatrix} \begin{bmatrix} \ddot{u}_b \\ \ddot{u}_f \end{bmatrix}}_{P_g^{\mathrm{iner}}} \right), \tag{14}$$

with the external and inertial loads P_g^{ext} and P_g^{iner} [37, 40]. The mass matrix M_{gg} is defined with respect to the structural grid and the rigid body acceleration $\ddot{u}_b$ is

$$\ddot{u}_b = \begin{bmatrix} \dot{V}_b + \Omega_b \times V_b - T_{be} g_e \\ \dot{\Omega}_b + J_b^{-1}(\Omega_b \times (J_b \Omega_b)) \end{bmatrix}. \tag{15}$$

Eventually, in Equation (14) the multiplication with matrix $T_{\mathrm{mx}g}$ sums the incremental loads of all grid points along the wing and transforms them to the loads coordinate system at the wing root.
Actuator and sensor models complete the aeroservoelastic model used for the synthesis and analysis of a GLA controller.

For further details on the structural and aerodynamic modelling of the FliPASED demonstrator aircraft it is referred to Refs. [10, 36, 39].

As for the aerofoil model various mass models are generated which represent different fuel levels of the wing tanks. The demonstrator aircraft does not really possess tanks in the wings.

That is why the loss of fuel mass along the wings is mimiced for study purposes. The virtual wing tanks are depicted in Figure 4 by grey boxes. Each box represents a discretised fuel mass with the centroid rigidly connected to the closest structural grid point. The mass moment of inertias are approximated by dividing the mass into four parts, shown as grey points, each attached to the corner of a section. The size of a section correlates with its mass. As the effect of a hanged mass on the structural modes increases along the wing span, the section size decays in a quadratic manner. Furthermore, due to aircraft stability reasons the tank sections are placed far from the wing roots. For the generation of the different mass cases it is assumed that the fuel is burnt from the most inner to the most outer section, i.e. bit by bit the section masses are removed until there is no fuel left. In total 11 mass cases, which are outlined in Table 2, are generated. Finally, the aeroservoelastic model is linearised for the different mass cases at

Table 2: Mass cases for the demonstrator aircraft.

Mass Case	Wing Fuel Mass [kg]	Total Mass [kg]
1	17.40	82.42
2	13.62	78.65
3	10.43	75.46
4	7.76	72.79
5	5.56	70.59
6	3.78	68.81
7	2.37	67.40
8	1.32	66.34
9	0.58	65.61
10	0.14	65.17
11	0.00	65.03

$U_\infty = 39.5\,\mathrm{m/s}$. This leads to a set of state-space models in the form of Equation (3).

2.3 Gust Model

Within the scope of this paper, the atmospheric disturbance is a discrete, vertical 1-cosine gust. It is defined by the gust zone velocity and acceleration $U_{z,\text{gust}}(t)$ and $\dot{U}_{z,\text{gust}}(t)$

$$
\begin{aligned}
U_{z,\text{gust}}(t) &= \begin{cases} \dfrac{U_{\text{gust,max}}}{2}\left(1-\cos\left(\dfrac{\pi}{H_{\text{gust}}}U_\infty t\right)\right), & \text{if } t_{z,1} \le t \le t_{z,\text{end}} \\ 0, & \text{otherwise} \end{cases} \\
\dot{U}_{z,\text{gust}}(t) &= \begin{cases} -\dfrac{U_{\text{gust,max}}\pi}{2H_{\text{gust}}}U_\infty \sin\left(\dfrac{\pi}{H_{\text{gust}}}U_\infty t\right), & \text{if } t_{z,1} \le t \le t_{z,\text{end}} \\ 0, & \text{otherwise,} \end{cases}
\end{aligned}
\tag{16}
$$

where $U_{\text{gust,max}}$ is the maximum gust intensity and H_{gust} the gust half length [41]. With increasing time t the aerofoil and aircraft move through the gust from nose to aft, like shown in Figures 3 and 5. For the aerofoil model the forces and moments induced by the gust act on the elastic axis e. Unsteady aerodynamics are neglected, i.e. the gust zone acceleration $\dot{U}_{z,\text{gust}}(t)$ has no effect and is disregarded. Differences in the forces and moments along the aerofoil caused by the 1-cosine gust profile are neglected as well, resulting in one gust zone over the entire aerofoil. The aerodynamic model of the demonstrator aircraft is divided in several gust zones like shown in Figure 5. The gust reaches the centre of a gust zone, depicted by the dashed vertical lines of the panel model, at time $t_{z,1}$ and leaves it at time $t_{z,\text{end}}$. All aerodynamic panels between

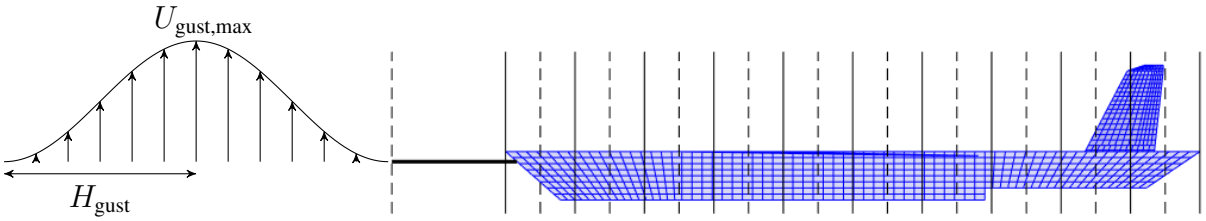

Figure 5: 1-cosine gust and aircraft gust zones [10].

the vertical solid lines of a gust zone are affected by the gust velocity observed at the centre. Namely, within a gust zone the gust velocity is constant. The airdata boom at the nose of the aircraft is specially treated and considered to be a zone for itself. Thus, changes in the angle of attack α due to an approaching gust are recognised before the gust hits the aircraft. This offers the opportunity to use a feedforward path increasing the reaction time [32]. The gust zone approach is an approximation which saves a lot of computation time, as it groups many aerodynamic panels into few zones. Furthermore, with ten gust zones it is an accurate enough implementation for the demonstrator aircraft [42]. The difference in the gust zone velocity of two neighbouring gust zones is caused by a time delay. The transfer function of a time delay is defined by

$$G_{z,\text{delay}}(s) = e^{-t_{z,\text{delay}}s}, \tag{17}$$

where $t_{z,\text{delay}}$ is the time delay in seconds and s is the Laplace variable [42]. Equation (17) is approximated by the second-order Padé approximation

$$G_{z,\text{delay}}(s) \approx \frac{s^2 - \frac{6}{t_{z,\text{delay}}}s + \frac{12}{t_{z,\text{delay}}^2}}{s^2 + \frac{6}{t_{z,\text{delay}}}s + \frac{12}{t_{z,\text{delay}}^2}}, \tag{18}$$

as it is convertable into state-space format and can be used with the set of linearised mass models [43].

3 GLA CONTROLLER SYNTHESIS

The GLA control synthesis is stated as an optimisation problem which is solved by using the Multi-Objective Parameter Synthesis (MOPS) tool [44]. Besides the set of multiple-model adaptive (MMA) GLA controllers, a reference GLA controller is synthesised. This allows to compare both control architectures and demonstrate the improvement MMAC has to offer.

3.1 Reference GLA Controller

The reference controller $\bar{K}_{\text{GLA}}$ uses global control (GC) that is supposed to robustly operate over the entire set of mass properties Ω_{p_m}. In Ref. [27] the robust controller $\bar{K}_{\text{GLA}}$ over Ω_{p_m} is therefore entitled *global non-adaptive robust compensator*. As previously stated, the set Ω_{p_m} is finely gridded resulting in an approximated subset $\tilde{\Omega}_{p_m}$. Furthermore, for the synthesis of $\bar{K}_{\text{GLA}}$ only the first, last and a few intermediate mass properties of $\tilde{\Omega}_{p_m}$ are regarded, in order to speed up the synthesis. As the mass models are selected with an incremental change in $p_{m,i}$ it is assumed that this is a valid approach. The reference controller $\bar{K}_{\text{GLA}}$ is then found through optimising the objective function $J(\bar{K}_{\text{GLA}})$ for the various mass models in parallel. A comparable approach is more deeply discussed in Ref. [31].

3.2 Mass Case Specific GLA Controller

Like previously stated, the potential of an MMAC architecture is a significant performance improvement. In order to investigate this circumstance, for each regarded mass case $p_{m,i} \in \tilde{\Omega}_{p_m}$ a controller $K_{\text{GLA},p_{m,i}}$ is specifically synthesised. This leads to a set of n_k, which is equal to n_m, controllers. The theory is that the finer the set of mass properties $\tilde{\Omega}_{p_m}$ is gridded, i.e. n_m increases, the closer one reaches the optimal possible performance for the chosen controller architecture and synthesis method over the considered parameter change [27]. Ref. [27] uses the term *fixed non-adaptive robust compensator* for the controllers $K_{\text{GLA},p_{m,i}}$ with $n_m \to \infty$. An admissible trade-off is to choose $n_m \gg 1$ for a manageable amount of controllers. The assessment of the objective function $J(K_{\text{GLA},p_{m,i}})$ and the constraints $c(K_{\text{GLA},p_{m,i}})$ for each mass case in closed-loop then demonstrates the improvement with respect to the closed-loop mass models augmented by $\bar{K}_{\text{GLA}}$.

3.3 Synthesis Method

The objective function $J(K_{\text{GLA}})$ and the constraints $c(K_{\text{GLA}})$ are the same for both, the global GLA controller $\bar{K}_{\text{GLA}}$ and the mass case specific set of controllers $K_{\text{GLA},p_{m,i}}$. Therefore, in the following the GLA controller is simply denoted by K_{GLA}. The sought-after control transfer function from the n_y controlled outputs y to the n_u controlled inputs u is of the form

$$K_{\text{GLA}}(s) = \begin{bmatrix} k_{11}\dfrac{\prod_{i=1}^{n_p-1}(s-z_{11,i})}{\prod_{i=1}^{n_p}(s-p_i)} & \dots & k_{1n_y}\dfrac{\prod_{i=1}^{n_p-1}(s-z_{1n_y,i})}{\prod_{i=1}^{n_p}(s-p_i)} \\ \vdots & \ddots & \vdots \\ k_{n_u1}\dfrac{\prod_{i=1}^{n_p-1}(s-z_{n_u1,i})}{\prod_{i=1}^{n_p}(s-p_i)} & \dots & k_{n_un_y}\dfrac{\prod_{i=1}^{n_p-1}(s-z_{n_un_y,i})}{\prod_{i=1}^{n_p}(s-p_i)} \end{bmatrix}, \tag{19}$$

where $k_{i_ui_y}$ and $z_{i_ui_y,i}$ with $i_u = 1, ..., n_u$ and $i_y = 1, ..., n_y$ are the gains and zeros and p_i are the poles to be defined [32]. The order of the numerator is $n_p - 1$ and therefore smaller than the order of the denominator n_p. Thereby, the controller transfer function $K_{\text{GLA}}(s)$ is strictly proper and guarantees a high frequency roll-off in the control action [10]. To simplify the optimisation problem the poles and zeros of Equation (19) are grouped in conjugate complex pairs

$$\begin{aligned} z_{i_ui_y,i/i+1} &= -\zeta_{i_ui_y,i}\omega_{n,i_ui_y,i} \pm \omega_{n,i_ui_y,i}\sqrt{1-\zeta_{i_ui_y,i}^2} \quad i = 1,3,\dots,n_p-3 \\ z_{i_ui_y,n_p-1} &= -\omega_{n,i_ui_y,n_p-1} \\ p_{i/i+1} &= -\zeta_i\omega_{n,i} \pm \omega_{n,i}\sqrt{1-\zeta_i^2} \quad i = 1,3,\dots,n_p-1 \end{aligned} \tag{20}$$

except for one real zero $z_{i_ui_y,n_p-1}$ for even n_p. For both the aerofoil ($n_p = 4$) and the demonstrator aircraft ($n_p = 8$) this is the case. Thus, only the gains $k_{i_ui_y}$, the natural frequencies $\omega_{n,i}$ and $\omega_{n,i_ui_y,i}$ and the damping ratios ζ_i and $\zeta_{i_ui_y,i}$ have to be determined. Furthermore, the feasible values of all damping ratios ζ is restricted to values between 0 and 1. The controller then only features poles and zeros that are in the left half plane.

Primary goal of the GLA control synthesis is to reduce the WRBM. Therefore, a family of gust encounters featuring n_{gust} different gust half lengths $H_{\text{gust},i}$ is simulated. With respect to the open-loop loads the closed-loop loads are to be minimised. The objective function is

$$J(K_{\text{GLA}}) = \min_{K_{\text{GLA}}} \frac{\max\limits_{i,t}(P_{x,\text{CL},i}(t)^2)}{\max\limits_{i,t}(P_{x,\text{OL},i}(t)^2)},\ i = 1,2,\dots,n_{\text{gust}}, \tag{21}$$

with $P_{x,\mathrm{CL},i}(t)$ and $P_{x,\mathrm{OL},i}(t)$ being the closed-loop and open-loop time simulations for the i^{th} gust half length. Dependent on the aforementioned examples, the considered loads will either be P_h or P_{mx}. In Equation (21), the loads are squared in order to penalise high negative and positive values equally. Therefore, an optimal controller K_{GLA} minimises the maximum squared loads of the closed-loop system with respect to the open-loop system.
Besides the objective function, constraints are defined to exclude infeasible solutions to the optimisation problem. The first constraint limits the relative difference between the closed-loop and the open-loop transfer function $G_{\mathrm{CL}}(K_{\mathrm{GLA}})$ and G_{OL} from gust input u_g to load output $P_{x,\mathrm{CL}}$ and $P_{x,\mathrm{OL}}$, respectively. This is especially wanted in low frequencies, so that the GLA controller does not affect the flight dynamics, and in high frequencies for little control action. These requirements yield the constraint

$$c_e(K_{\mathrm{GLA}}) = ||\frac{1}{e_{\max}} W_{e1} W_{e2} \left(G_{\mathrm{CL}}(K_{\mathrm{GLA}}) - G_{\mathrm{OL}}\right) / G_{\mathrm{OL}}||_\infty \leq 1. \tag{22}$$

The weighting functions W_{e1} and W_{e2} put emphasis on very low and very high frequencies for which a maximum relative difference can be defined with $e_{\max}$ [10]. It is 0.05 for the GLA controller synthesis for the aerofoil and 0.1 for the demonstrator aircraft. Equation (22) is separated in two constraints for the aerofoil model. This is necessary as the GLA control for the aerofoil is meant to happen in a quite narrow frequency band and the separation of the requirements for low and high frequencies is numerically more convenient.
Moreover, the closed-loop system needs to be stable. That is why the closed-loop pole featuring the smallest damping ratio is restricted to be in the left half plane with a lower bound b_ζ. The second constraint therefore is

$$c_\zeta(K_{\mathrm{GLA}}) = \zeta_{\mathrm{CL,min}}(K_{\mathrm{GLA}}) \geq b_\zeta \geq 0. \tag{23}$$

For the aerofoil and the FliPASED demonstrator aircraft the safety bound is chosen as $b_\zeta = 0.01$. Lastly, a constraint is put on the relation between the closed-loop and open-loop maximum root mean square (RMS) of all gust simulations [45]. This demands a certain decay rate for the closed-loop loads $P_{x,\mathrm{CL},i}(t)$ after a gust encounter. This constraint is given by

$$c_{\mathrm{rms}}(K_{\mathrm{GLA}}) = \frac{\max\limits_i \left(\frac{1}{n_{\mathrm{end}}} \sum_{k=1}^{n_{\mathrm{end}}} P_{x,\mathrm{CL},i}(t_k, K_{\mathrm{GLA}})^2\right)}{\max\limits_i \left(\frac{1}{n_{\mathrm{end}}} \sum_{k=1}^{n_{\mathrm{end}}} P_{x,\mathrm{OL},i}(t_k)^2\right)} \leq b_{\mathrm{rms}}^2 \leq 1,\ i = 1, \ldots, n_{\mathrm{gust}}. \tag{24}$$

The upper bound b_{rms} limits the closed-loop RMS. For the aerofoil example b_{rms} is equal to 1, while for the FliPASED demonstrator aircraft it is 0.98.

The optimisation is performed with a genetic algorithm, that is followed by a pattern search for the last iterations [44, 46, 47].
Firstly, the global robust $\bar{K}_{\mathrm{GLA}}$ is synthesised over all mass cases. The resulting controller $\bar{K}_{\mathrm{GLA}}$ is used as an initial guess for the optimisation of the first considered mass case with mass properties $p_{m,1} = p_{m,\mathrm{high}}$. The optimal controller of mass case $p_{m,\mathrm{i}}$ then represents the initial controller estimation for the subsequent mass case $p_{m,\mathrm{i+1}}$. Thereby, the optimisation is started with promising control parameters as the mass changes are small.

As stated above, for all aerofoil mass models a true airspeed $U_\infty = 10\,\mathrm{m/s}$ is assumed. The outputs fed to the controller are the states $y = x = \begin{bmatrix} h & \alpha & \dot{h} & \dot{\alpha} \end{bmatrix}^T$. Based on these signals the controller then generates a control surface deflection $u = u_\delta$.

The true airspeed for the demonstrator aircraft is fixed to $U_\infty = 39.5\,\mathrm{m/s}$, i.e. an indicated airspeed of $U_{\mathrm{IAS}} = 38\,\mathrm{m/s}$. The measurements and control inputs for the GLA control are depicted in Figure 6 where the relevant control surfaces and inertial measurement units (IMUs) are highlighted in green and red, respectively. The GLA controller processes the α measurement

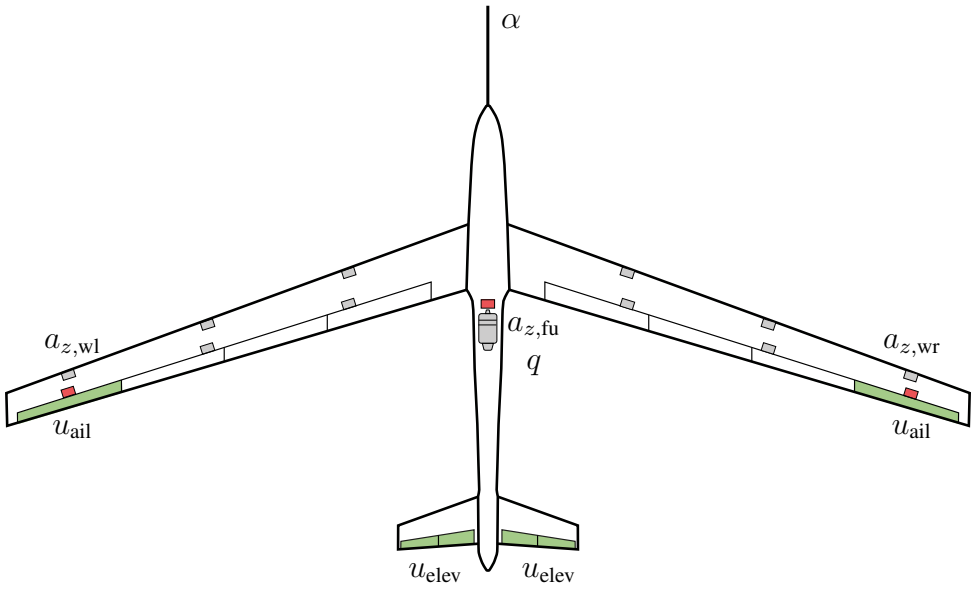

Figure 6: Demonstrator aircraft with IMUs (red) and control surfaces (green) for GLA control [48].

of the air data boom at the nose, the pitch rate q and the vertical accelerations $a_{z,\mathrm{fu}}$, $a_{z,\mathrm{wl}}$ and $a_{z,\mathrm{wr}}$ of the IMUs in the fuselage and on the left and right wing. The controller calculates commanded deflections to the most outer ailerons of the wings u_{ail} and the elevators u_{elev}. Thus, one deflection signal u_{ail} connected to both ailerons and one deflection signal u_{elev} connected to all four elevators are fed to the control surfaces. This combination of signals is valid as the aircraft is nearly symmetric and only vertical gust encounters are considered. For the synthesis of the GLA controllers it is decided to exclude unsteady gust aerodynamics, however they are taken into account for the subsequent analysis.

4 ANALYSIS OF THE MMA GLA CONTROL ARCHITECTURE

In the analysis of the GLA control application, the focus is on the comparison of the system performance of the open-loop system compared to the closed-loop system with the global robust controller $\bar{K}_{\mathrm{GLA}}$ and with the mass case specific controllers $K_{\mathrm{GLA},p_{m,i}}$. The performance is measured based on the square root of the objective function value, i.e. the relative reduction of the absolute loads. Furthermore, the constraints must not be violated. To unify their assessment Equations (23) and (24) are transformed to constraints which need to be less or equal to 1, which is already the case for c_e in Equation (22). Thus, only the worst case value of the constraints is of relevance yielding

$$c_{\max} = \max\left(c_e(K_{\mathrm{GLA}}), 1 + b_\zeta - c_\zeta(K_{\mathrm{GLA}}), \frac{c_{\mathrm{rms}}(K_{\mathrm{GLA}})}{b_{\mathrm{rms}}^2}\right) \leq 1. \tag{25}$$

The analysis of the models with mass properties $p_{m,i} \in \tilde{\Omega}_{p_m}$ then provides information on which mass cases are specifically relevant for MMAC.

4.1 GLA Controller Analysis for the Aerofoil Model

For the aerofoil model 22 mass cases are considered. In Figure 7 the loads P_h for a family of different gust half lenghts H_{gust} between 1 and 5 m are simulated for mass case 1, 11 and 22. The

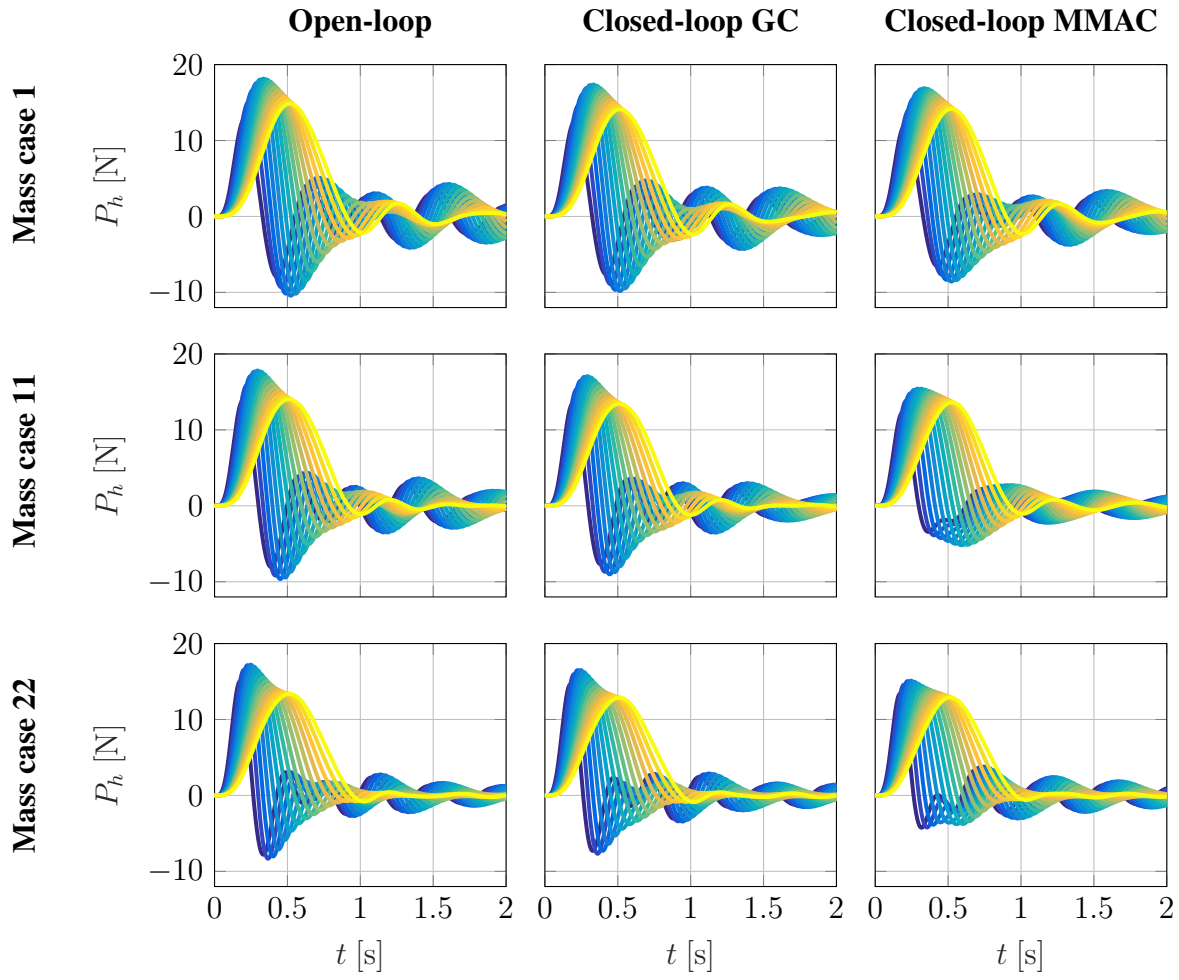

Figure 7: Open- and closed-loop gust simulations of the aerofoil for $H_{\text{gust}} = 1\,\text{m}$ to $5\,\text{m}$.

left column represents the open-loop system, while the middle and right column depict P_h for the closed-loop system with the global controller $\bar{K}_{\text{GLA}}$ and the mass case specific controllers $K_{\text{GLA},p_{m,i}}$, respectively. For all considered mass cases a reduction of the maximum absolute loads in closed-loop can be recognised, which is higher for the MMA GLA than for the global GLA. From mass case 1 to mass case 22 the performance improvement even intensifies for MMAC. In the upper part of Figure 8 the actual improvement relative to the open-loop case is depicted over all 22 mass cases. While the GC, depicted in blue, offers a more or less mass independent load reduction of approximately 4 %, the MMAC architecture, in green, clearly exhibits a performance benefit of 7 % up to 13 % over the mass cases. The lower part of Figure 8 shows the maximum constraint c_{max} which should be less or equal to one. Higher values indicate that at least one constraint has been violated. As it can be seen, this is the case for some mass cases with MMAC due to a tight constraint c_e for high frequencies. As the frequency band for GLA control is narrow, which leads to high order weighting functions W_{e1} and W_{e2}, the genetic algorithm has difficulties to cope with the optimisation problem. Generally, genetic algorithms are not very appropriate for constrained optimisation problems, which is why constraints might

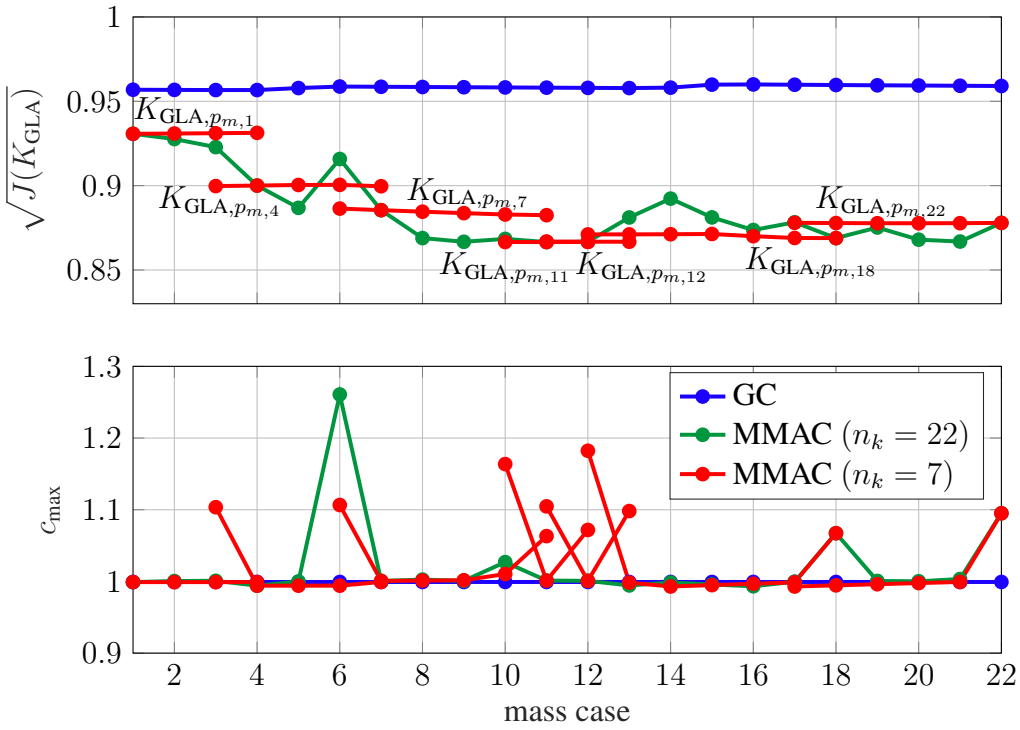

Figure 8: Performance assessment and controller selection for the aerofoil model.

be violated [49]. Nevertheless, based on the controllers $K_{\text{GLA},p_{m,i}}$ and Figure 8 a decision can be made which controllers to choose as a minimum and still benefit from the performance improvement of MMAC. In an analysis each controller $K_{\text{GLA},p_{m,i}}$ is connected to the various mass case models and their performance and constraint violation is assessed. It is found that controllers synthesised for mass case 1, 4, 7, 11, 12, 18 and 22 provide an appropriate set of GLA controllers. The operating point of the set of controllers with respect to mass is shown in red in Figure 8. Thus, for the range of the $n_m = 22$ mass cases a selection of $n_k = 7$ controllers is sufficient. For some mass cases, like e.g. 14, the chosen controller lead to an even better performance than the one especially synthesised for the dedicated mass case. This shows that the optimisation problem is highly non-convex and that even the global optimsation might not lead to the optimal solution. The selection of controllers is mainly driven by the violation of constraint c_e, i.e. as soon as a selected controller causes the closed-loop system to not fulfil the constraint for a specific mass case, a more convenient controller needs to be selected. However, mass case 22 cannot be kept within the constraints with any of the synthesised controllers. This is also challenging for mass cases 9 to 13. For each a controller can be found which keeps $c_{\max}$ at least nearly to 1. However, for intermediate mass properties the constraint c_e would definitely be violated.

4.2 GLA Controller Analysis for the FliPASED Demonstrator Aircraft

As for the aerofoil model, GLA controllers for the 11 mass cases from Table 2 are synthesised for GC and MMAC. The resulting time simulations for mass cases 1, 5 and 11 are given in Figure 9. As can be seen, the negative WRBM loads P_{mx} are especially large. Like for the aerofoil, the MMAC architecture also demonstrates its performance benefits for the demonstrator aircraft. The relative improvement increases over the mass cases. In Figure 10 the performance relative to the open-loop case is displayed. Like for the aerofoil, the GC features a more or less constant load reduction of 10 %, while the MMAC architecture clearly offers a performance benefit with increasing mass case of approximately 20 % load reduction. It can be seen that the

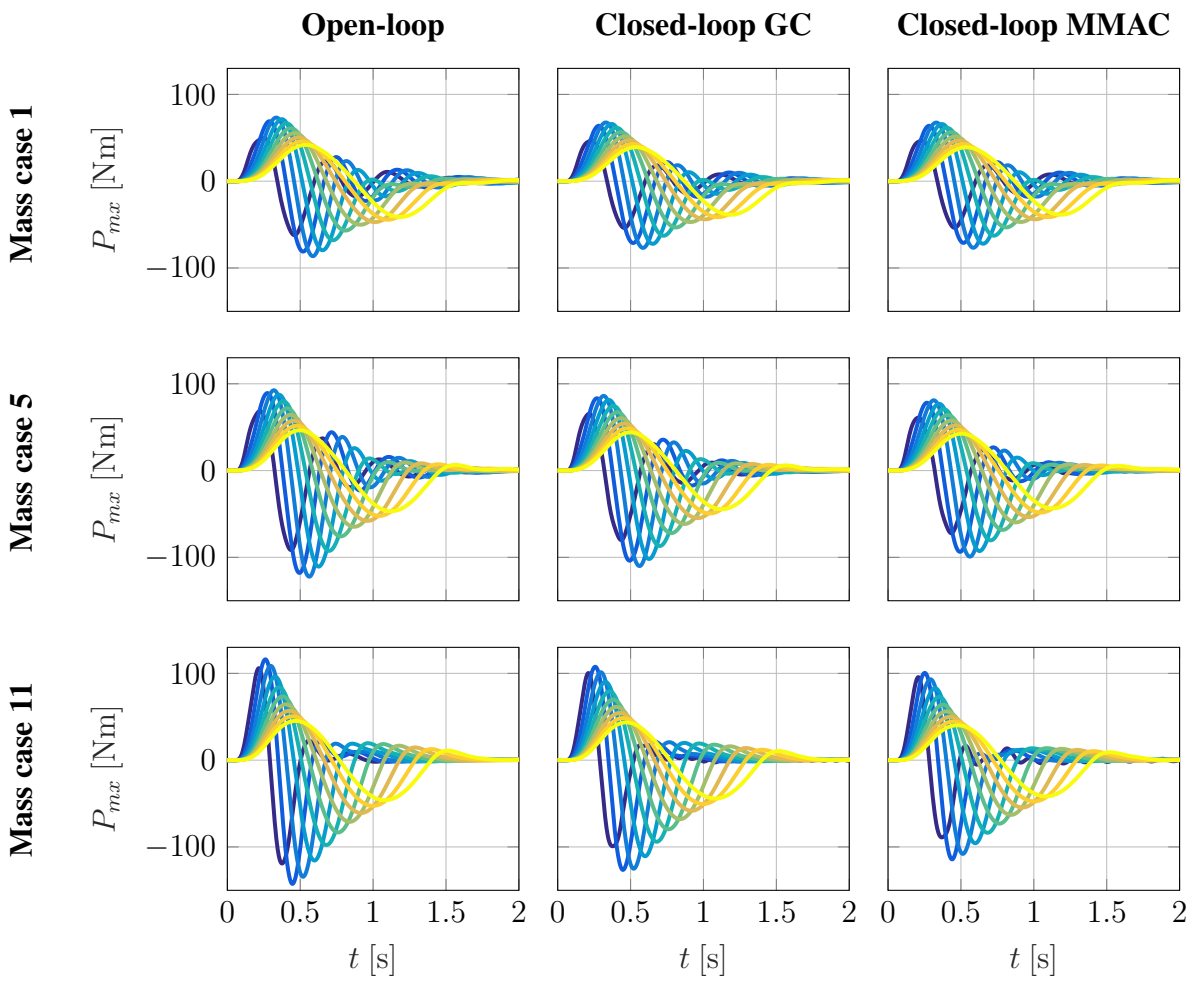

Figure 9: Open- and closed-loop gust simulations of the demonstrator aircraft for $H_{\text{gust}} = 4\,\text{m}$ to $25\,\text{m}$.

constraint c_{max} is less sensitive than for the aerofoil and $n_k = 4$ controllers from mass cases 1, 3, 6 and 9 can be found fulfilling the requirements. As well as for the aerofoil, the performance with MMAC can even be exceeded with the four selected controller around mass case 8.

5 CONCLUSION AND OUTLOOK

Aeroelastic models are set up for a two-degree-of-freedom aerofoil model and the FliPASED demonstrator aircraft. In order to imitate the fuel consumption within flight a set of models with changing mass properties is defined. GLA control is then performed for the set of models and the benefit of an MMAC over a GC architecture is illustrated. The gust loads for both, the aerofoil model and the FliPASED demonstrator aircraft, can be further improved with MMAC. For the aerofoil the reduction of loads with a GC amounts approximately $4\,\%$, while with MMAC it is enhanced to $7\,\%$ up to $13\,\%$. GC applied to the demonstrator aircraft offers a load reduction of $10\,\%$. For MMAC it roughly equals the performance of the GC for the first mass cases and reaches a maximum of more or less $20\,\%$. Based on the analysis performed a minimum number of controllers for MMAC is selected, which is 7 for the aerofoil and 4 for the demonstrator aircraft. A next step would involve the identification of the mass case that represents the current state of the system best and the switching to the corresponding controller. The optimisation problem could be further simplified featuring less parameters, as it is highly non-convex and even the chosen genetic algorithm has difficulties to find the optimal solution. Finally, robust-

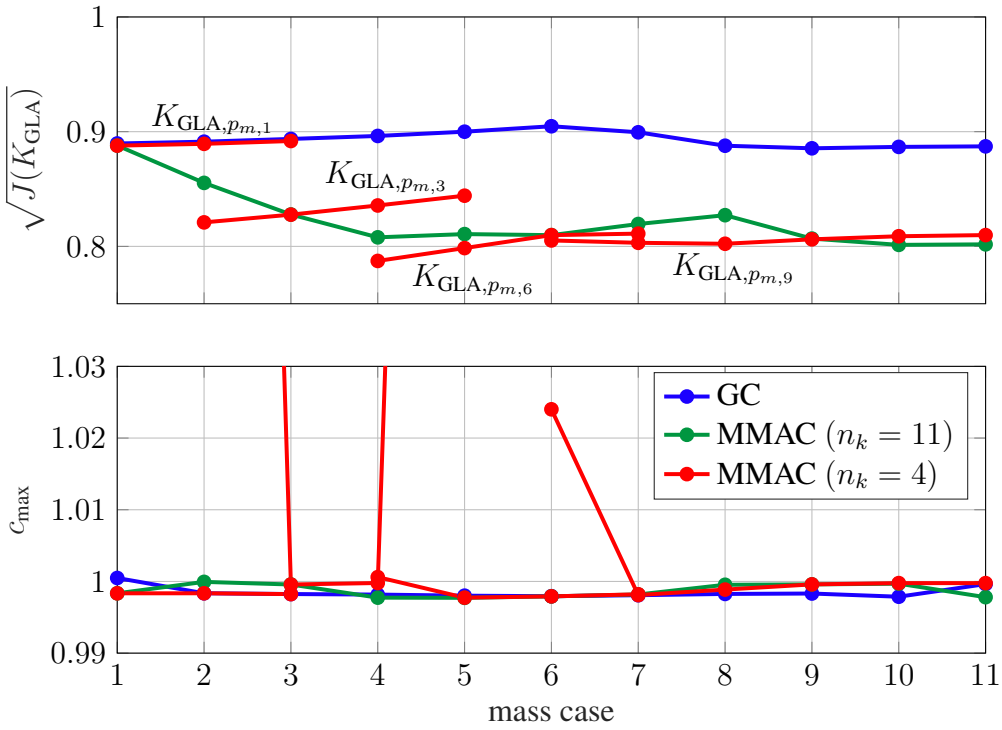

Figure 10: Performance assessment and controller selection for the demonstrator aircraft.

ness, which is not proven in this paper, has to be guaranteed. Subsequent to the synthesis of the GLA controllers an anti-optimisation for the given objective function and constraints could be performed to find the worst case scenario with respect to uncertainties in the modelling. This kind of robustness analysis has been documented in Ref. [50].

ACKNOWLEDGMENTS

The research leading to these results is part of the FLiPASED project. This project has received funding from the European Unions Horizon 2020 research and innovation program under grant agreement No. 815058.
Special thanks go to my colleagues Reiko Müller, Peter Eschenbacher and Carsten Oldemeyer for inspiring discussions and valuable advice that made this work possible.

6 REFERENCES

[1] International Energy Agency (2009). *Transport, Energy and CO_2: Moving toward sustainability*. Paris: International Energy Agency. ISBN 9264073167.

[2] Livne, E. (2018). Aircraft active flutter suppression: State of the art and technology maturation needs. *Journal of Aircraft*, 55(1), 410–452. ISSN 0021-8669. doi: 10.2514/1.C034442.

[3] Wright, J. R. and Cooper, J. E. (2015). *Introduction to Aircraft Aeroelasticity and Loads*. Chichester UK: John Wiley & Sons, Ltd, 2 ed.

[4] Regan, C. D. and Jutte, C. V. (2012). Survey of applications of active control technology for gust alleviation and new challenges for lighter-weight aircraft. (DFRC-E-DAA-TN4736).

[5] Burlion, L., Poussot-Vassal, C., Vuillemin, P., et al. (2014). Longitudinal manoeuvre load control of a flexible large-scale aircraft. In E. Boje (Ed.), *Proceedings of the 19th IFAC World Congress 2014*, vol. 19. pp. 3413–2418.

[6] Mancini, A. and Vos, R. (2019). The effect of maneuver load alleviation strategies on aircraft performance indicators. In *AIAA Aviation 2019 Forum*. Reston, Virginia: American Institute of Aeronautics and Astronautics. ISBN 978-1-62410-589-0, p. 3453. doi: 10.2514/6.2019-3272.

[7] Poussot-Vassal, C., Vuillemin, P., Cantinaud, O., et al. (2021). Interpolatory methods for generic bizjet gust load alleviation function (accepted). *SIAM Journal on Applied Dynamical Systems*.

[8] Binder, S. (2021). *Simultaneous Optimisation of Composite Wing Structures and Control Systems for Active and Passive Load Alleviation*. Dissertation, Delft University of Technology, Delft. doi:10.4233/UUID:FAC93CCF-7E0B-4971-A797-D2617E378A1D.

[9] Capello, E., Guglieri, G., and Quagliotti, F. (2014). L1 adaptive controller design for gust load alleviation. In *29th Congress of the International Council of the Aeronautical Sciences (ICAS 2014)*. International Council of The Aeronautical Sciences (ICAS). ISBN 9781634394116.

[10] Wuestenhagen, M. (2022). Synthesis of a multiple-model adaptive gust load alleviation controller for a flexible flutter demonstrator. In *AIAA Scitech 2022 Forum*. Reston, Virginia: American Institute of Aeronautics and Astronautics, p. 4439. doi: 10.2514/6.2022-0440.

[11] Flight phase adaptive aero-servo-elastic aircraft design methods. url: https://cordis.europa.eu/project/id/815058

[12] Flexop. url: https://flexop.eu/

[13] Stahl, P., Sendner, F.-M., Hermanutz, A., et al. (2017). Mission and aircraft design of flexop unmanned flying demonstrator to test flutter suppression within visual line of sight. In *17th AIAA Aviation Technology, Integration, and Operations Conference*. Reston, Virginia: American Institute of Aeronautics and Astronautics. ISBN 978-1-62410-508-1. doi:10.2514/6.2017-3766.

[14] Rößler, C., Stahl, P., Sendner, F., et al. (2019). Aircraft design and testing of flexop unmanned flying demonstrator to test load alleviation and flutter suppression of high aspect ratio flexible wings. In *AIAA Scitech 2019 Forum*. Reston, Virginia: American Institute of Aeronautics and Astronautics. ISBN 978-1-62410-578-4. doi:10.2514/6.2019-1813.

[15] Meddaikar, Y. M., Dillinger, J., Klimmek, T., et al. (2019). Aircraft aeroservoelastic modelling of the flexop unmanned flying demonstrator. In *AIAA Scitech 2019 Forum*. Reston, Virginia: American Institute of Aeronautics and Astronautics. ISBN 978-1-62410-578-4. doi:10.2514/6.2019-1815.

[16] Takarics, B., Patartics, B., Luspay, T., et al. (2020). Active flutter mitigation testing on the flexop demonstrator aircraft. In *AIAA Scitech 2020 Forum*. Reston, Virginia: American Institute of Aeronautics and Astronautics. ISBN 978-1-62410-595-1. doi: 10.2514/6.2020-1970.

[17] Rößler, C., Bartasevicius, J., Köberle, S., et al. (2020). Results of an aeroelastically tailored wing on the flexop demonstrator aircraft. In *AIAA Scitech 2020 Forum*. Reston, Virginia: American Institute of Aeronautics and Astronautics. ISBN 978-1-62410-595-1. doi:10.2514/6.2020-1969.

[18] Knoblach, A. (2015). *Robust Performance Analysis for Gust Loads Computation: Dissertation*. München: Verlag Dr. Hut. ISBN 978-3-8439-2251-7.

[19] Landau, I. D., Lozano, R., M'Saad, M., et al. (2011). *Adaptive Control*. London, UK: Springer London, 2 ed. ISBN 978-0-85729-663-4. doi:10.1007/978-0-85729-664-1.

[20] Lin, Z. (2002). *Gain scheduling of aircraft pitch attitude and control of discrete, affine, linear parametrically varying systems*. Dissertation, Iowa State University, Ann Arbor, Mi. doi:10.31274/rtd-180813-11950.

[21] Aouf, N., Boulet, B., and Botez, R. (08.05.2002 - 10.05.2002). A gain scheduling approach for a flexible aircraft. In *Proceedings of the 2002 American Control Conference (IEEE Cat. No.CH37301)*. IEEE. ISBN 0-7803-7298-0, pp. 4439–4442 vol.6. doi:10.1109/ACC.2002.1025347.

[22] Fan, W., Liu, H. H. T., and Kwong, R. H. S. (2017). Gain-scheduling control of flexible aircraft with actuator saturation and stuck faults. *Journal of Guidance, Control, and Dynamics*, 40(3), 510–520. ISSN 0731-5090. doi:10.2514/1.G002222.

[23] Ballauf, C. (2008). *Dämpfung aeroelastischer Strukturen mit modelladaptiver Regelung: Zugl.: München, Techn. Univ., Diss., 2008*, vol. 1155 of *Fortschrittberichte VDI Reihe 8, Mess-, Steuerungs- und Regelungstechnik*. Düsseldorf: VDI-Verl., als ms. gedr ed. ISBN 9783185155086.

[24] Rohrs, C., Valavani, L., Athans, M., et al. (1985). Robustness of continuous-time adaptive control algorithms in the presence of unmodeled dynamics. *IEEE Transactions on Automatic Control*, 30(9), 881–889. ISSN 00189286. doi:10.1109/TAC.1985.1104070.

[25] Morse, A. S. (Ed.) (1997). *Control Using Logic-Based Switching*. London, UK: Springer London. ISBN 3540760970.

[26] Narendra, K. S. and Balakrishnan, J. (1997). Adaptive control using multiple models. *IEEE Transactions on Automatic Control*, 42(2), 171–187.

[27] Fekri, S., Athans, M., and Pascoal, A. (2006). Issues, progress and new results in robust adaptive control. *International Journal of Adaptive Control and Signal Processing*, 20(10), 519–579. ISSN 08906327. doi:10.1002/acs.912.

[28] Galán, O., Romagnoli, J. A., and Palazoglu, A. (2000). Robust h infinity control of nonlinear plants based on multi-linear models: an application to a bench-scale ph neutralization reactor. *Chemical Engineering Science*, 55(20), 4435–4450. ISSN 00092509. doi:10.1016/S0009-2509(00)00028-2.

[29] Bhagwat, A., Srinivasan, R., and R. Krishnaswamy, P. (2003). Multi-linear model-based fault detection during process transitions. *Chemical Engineering Science*, 58(9), 1649–1670. ISSN 00092509. doi:10.1016/S0009-2509(03)00008-3.

[30] Anderson, B. D. O., Brinsmead, T. S., de Bruyne, F., et al. (2000). Multiple model adaptive control. part 1: Finite controller coverings. *International Journal of Robust and Nonlinear Control*, 10, 909–929. ISSN 10498923.

[31] Fezans, N., Joos, H.-D., and Deiler, C. (2019). Gust load alleviation for a long-range aircraft with and without anticipation. *CEAS Aeronautical Journal*, 10(4), 1033–1057. ISSN 1869-5582. doi:10.1007/s13272-019-00362-9.

[32] Skogestad, S. and Postlethwaite, I. (2005). *Multivariable Feedback Control: Analysis and design*. John Wiley and Sons, 2 ed. ISBN 978-0-470-01168-3.

[33] Ko, J., Kurdila, A. J., and Strganac, T. W. (1997). Nonlinear control of a prototypical wing section with torsional nonlinearity. *Journal of Guidance, Control, and Dynamics*, 20(6), 1181–1189. ISSN 0731-5090. doi:10.2514/2.4174.

[34] Zhang, R. and Singh, S. N. (2001). Adaptive output feedback control of an aeroelastic system with unstructured uncertainties. *Journal of Guidance, Control, and Dynamics*, 24(3), 502–509. ISSN 0731-5090. doi:10.2514/2.4739.

[35] GUYAN, R. J. (1965). Reduction of stiffness and mass matrices. *AIAA Journal*, 3(2), 380. ISSN 0001-1452. doi:10.2514/3.2874.

[36] Wüstenhagen, M., Kier, T., Meddaikar, Y. M., et al. (2018). Aeroservoelastic modeling and analysis of a highly flexible flutter demonstrator. In *2018 Atmospheric Flight Mechanics Conference*. Reston, Virginia: American Institute of Aeronautics and Astronautics. ISBN 978-1-62410-557-9. doi:10.2514/6.2018-3150.

[37] Kier, T. and Looye, G. (2009). Unifying manoeuvre and gust loads analysis models. In *International Forum on Aeroelasticity and Structural Dynamics*.

[38] Kier, T. and Hofstee, J. (2004). Varloads - eine simulationsumgebung zur lastenberechnung eines voll flexiblen, freifliegenden flugzeugs. In *Deutscher Luft- und Raumfahrtkongress*.

[39] Wüstenhagen, M., Süelözgen, Ö., Ackermann, L., et al. (2021). Validation and update of an aeroservoelastic model based on flight test data: 6-13 march 2021. In *2021 IEEE Aerospace Conference (50100)*. IEEE. doi:10.1109/AERO50100.2021.9438354.

[40] Bisplinghoff, R. L., Ashley, H., and Halfman, R. L. (1955). *Aeroelasticity*. Dover Publications, Inc. ISBN 978-0201005950.

[41] European Aviation Safety Agency (2007). Certification specifications for large aeroplanes (cs-25).

[42] Karpel, M., Moulin, B., and Chen, P. C. (2005). Dynamic response of aeroservoelastic systems to gust excitation. *Journal of Aircraft*, 42(5), 1264–1272. ISSN 0021-8669. doi:10.2514/1.6678.

[43] Hanta, V. and Procházka, A. (2009). Rational approximation of time delay.

[44] Joos, H.-D. (1999). A methodology for multi-objective design assessment and flight control synthesis tuning. *Aerospace Science and Technology*, 3(3), 161–176. ISSN 12709638. doi:10.1016/S1270-9638(99)80040-6.

[45] Rennie, R. and Law, J. (2019). *A Dictionary of Physics*. Oxford University Press, 6 ed. ISBN 9780199233991.

[46] Deb, K., Pratap, A., Agarwal, S., et al. (2002). A fast and elitist multiobjective genetic algorithm: Nsga-ii. *IEEE Transactions on Evolutionary Computation*, 6(2), 182–197. doi:10.1109/4235.996017.

[47] Hooke, R. and Jeeves, T. A. (1961). "direct search" solution of numerical and statistical problems. *Journal of the ACM*, 8(2), 212–229.

[48] Manuel Pusch (2020). *Blending of Inputs and Outputs for Modal Control of Aeroelastic Systems: Dissertation*. München: Verlag Dr. Hut. ISBN 978-3-8439-4661-2.

[49] Eiben, A. E. and Smith, J. E. (2015). *Introduction to Evolutionary Computing*. Berlin, Heidelberg: Springer Berlin Heidelberg, 2 ed. ISBN 978-3-662-44873-1. doi:10.1007/978-3-662-44874-8.

[50] Joos, H.-D. and Pfifer, H. (2012). Robust flight control system design verification and validation by multiobjective worst-case search. In *AIAA Guidance, Navigation, and Control Conference*. Reston, Virginia: American Institute of Aeronautics and Astronautics. ISBN 978-1-60086-938-9. doi:10.2514/6.2012-4998.

COPYRIGHT STATEMENT